Originally published as:

Geophysical Journal International

Spectral-finite element approach to viscoelastic relaxation in a spherical compressible Earth: application to GIA modelling

Y. Tanaka,[1] V. Klemann,[2] Z. Martinec[3,4] and R. E. M. Riva[5]

[1]*Earthquake Research Institute, University of Tokyo, 1-1-1 Yayoi, Bunkyo-ku, Tokyo 113-0032, Japan. E-mail: y-tanaka@eri.u-tokyo.ac.jp*
[2]*GFZ German Research Centre for Geosciences, Telegrafenberg, D-14473 Potsdam, Germany*
[3]*Dublin Institute for Advanced Studies, 5 Merriam Square, Dublin 2, Ireland*
[4]*Charles University, V Holešovičkách 2, 180 00 Prague 8, Czech Republic*
[5]*Delft Institute of Earth Observation and Space Systems (DEOS), Delft University of Technology, Klyuverweg 1, 2629 HS Delft, the Netherlands*

SUMMARY
The choice of the physical model of postglacial rebound plays a decisive role to derive information about the mantle rheology and viscosity from observed data. In models for the mantle rheology, an incompressible Maxwell material is often assumed in spite of seismic observations showing that the Earth's mantle is composed of compressible material. In this study, in order to assess the influence of compressibility on glacial isostatic adjustment (GIA), the spectral-finite element approach proposed by Martinec is extended to incorporate the effect of compressibility. Using this approach, the present-day velocity field is computed for Peltier's ICE5G/VM2 earth-model/glaciation-history combination considering the sea level equation in the formulation of Hagedoorn *et al*. The results show that the effect of compressibility on the vertical displacement rate is small whereas the horizontal rates are markedly enhanced. For example, the rate around Fennoscandia and Laurentide becomes twice as large when compressibility is considered. This large difference between the compressible and incompressible models can be reduced by adjusting the elastic rigidity of the incompressible model so that the flexural rigidity becomes approximately the same as that in the compressible model. However, differences of ∼1 mm yr^{-1} still remain for wavelengths longer than 8000 km. These findings show that when modelling horizontal motion induced by GIA, the influence of compressibility cannot be neglected.

Key words: Transient deformation; Global change from geodesy; Glaciology; Tectonics and climatic interactions; Dynamics of lithosphere and mantle; Rheology: mantle.

1 INTRODUCTION

Advances in space-geodetic observation systems such as GPS and GRACE have provided us with surface velocities and gravity data of unprecedented accuracy (Beutler *et al.* 2005). The interpretation of these data needs the separation of different contributions from the atmosphere, hydrosphere, cryosphere and solid Earth. The main contribution of the solid Earth from regional to global scales is associated with ongoing glacial isostatic adjustment (GIA) and the current ice-mass changes (Peltier 1998). It is well known that postglacial rebound can be viewed as the viscoelastic response of the Earth to a surface load. The demand on precise correction models for GIA motivates the improvement of rebound models considering different aspects of the mechanical and rheological behaviour of the solid Earth (e.g. Wu & Peltier 1982; Wolf 1985; Sabadini *et al.* 1986; Wolf 1991, 1994; Vermeersen *et al.* 1996; Kaufmann *et al.* 1997; Vermeersen & Sabadini 1997; Kaufmann & Wolf 1999; Tromp & Mitrovica 2000; Wolf & Kaufmann 2000; Martinec *et al.* 2001; Wolf & Li 2002; Steffen *et al.* 2006). There, the aspect of considering compressibility has been one issue for modelling postglacial rebound. Seismic observations show that the Earth's mantle is composed of compressible material (e.g. Karato 2003). Many theoretical studies have discussed the effects of compressibility so far (e.g. Wolf 1985, 1991; Vermeersen *et al.* 1996; Wolf & Li 2002; Klemann *et al.* 2003; Tanaka *et al.* 2009). However, a standard strategy for the implementation of the effect of compressibility in GIA is not yet accepted. In most GIA models, compressibility is often neglected (i.e. the kinematic constraint of div**u** = 0, where **u** is displacement, has been imposed) or approximated (e.g. Wolf 1991; Klemann *et al.* 2003; Wang *et al.* 2008), because of the following two problems (e.g. Han & Wahr 1995; Plag & Jüttner 1995).

The first problem is associated with the numerical handling of eigenmodes which appear in the presence of compressibility. The traditional approach to compute a viscoelastic relaxation, which has been used since Peltier (1974), is a normal mode method based on

an eigenmode expansion in the Laplace domain (e.g. Wu & Peltier 1982; Tromp & Mitrovica 1999). When compressibility is considered, denumerably infinite sets of modes appear in addition to the usual relaxation modes, which complicates the determination of the closed set of eigenmodes by numerical methods (e.g. Han & Wahr 1995).

This problem can be avoided by numerical approaches performed in the time domain such as an initial value technique (Hanyk *et al.* 1998; Martinec 1999) and a finite-element method (e.g. Wu 1999; Zhong *et al.* 2003; Steffen *et al.* 2006; Wu & Wang 2008) or a numerical inverse Laplace integration method (Tanaka *et al.* 2009). For a 1-D spherically symmetric model, Tanaka *et al.* (2009) shows theoretically that the effect of compressibility on the load Love numbers are detectable by current space techniques. For an earth model with a small number of layers, an analytical approximation method (Vermeersen *et al.* 1996) can also be used to evaluate these eigenmodes.

The second problem is associated with the choice of a reference-state model (e.g. Plag & Jüttner 1995; Hanyk *et al.* 1999). When compressibility is considered in a self-gravitating stratified earth model which violates the Adams–Williamson condition such as PREM (Dziewonski & Anderson 1981), modes with positive eigenvalues appear on timescales longer than geological ones (Vermeersen & Mitrovica 2000). This problem remains even if the above numerical approaches are employed (Hanyk *et al.* 1999; Tanaka *et al.* 2009). Vermeersen & Mitrovica (2000) show that these physical instabilities are of no influence when modelling GIA because their timescale is by orders of magnitude larger than the glaciation process, and so, their influence can be neglected with confidence. In Tanaka *et al.* (2009), the instability modes are included in order to keep the consistency between the elastic response computed with their method and a result by a time-domain approach. This takes the same position as in Plag & Jüttner (1995), who mentioned that the linear theory is valid on timescales shorter than the growth of an instability. Theoretical studies dealing with the instability modes are still continued (e.g. Cambiotti & Sabadini 2009). In addition, when using the normal mode method, a numerical instability associated with matrix inversion can arise in computations of viscoelastic deformation for long-time period (see Section 3.3).

On the other hand, the effect due to lateral heterogeneities has also become an important factor in the modelling of GIA, accompanied with the development of global seismic and geodetic observation networks [e.g. Kaufmann & Wu (1998, 2002), Marotta & Sabadini (2004), Wu (2005), Kaufmann *et al.* (2005) and Steffen *et al.* (2006) for half-space models and Latychev *et al.* (2005), Wang & Wu (2006a,b), Whitehouse *et al.* (2006) and Klemann *et al.* (2007, 2008) for spherical models]. In this respect, a finite-element approach is superior in that it allows handling strong lateral heterogeneities that cannot easily be treated by analytical methods (e.g. Wang 1991; Martinec & Wolf 1999; Zhong *et al.* 2003). However, extensive computational cost is required when setting up a 3-D finite-element mesh for global modelling. Hence, in most finite-element computations, a half-space model is employed to model local deformations and self-gravitation effects are treated approximately.

In this paper, we generalize the rheological model adopted in the spectral-finite element method of Martinec (2000) to a compressible case [note that the meaning of the term 'spectral' used here is different from that used in well known spectral-element methods (e.g. Komatitsch & Tromp 2002; Chaljub *et al.* 2003; Métivier *et al.* 2006)]. The characteristics of this approach are (1) an initial-value method in the time domain is employed and (2) finite elements are introduced in the radial direction only and the horizontal dependences are treated by tensor spherical harmonics. Applying a time-domain approach, we avoid to identify a large set of eigenmodes in the Laplace domain that originate from a realistic earth model structure like PREM. Introducing 1-D finite elements, discontinuities in the radial direction in the Earth structure can easily be treated, compared to the normal mode method based on integration or propagation techniques. Using spherical harmonics representing the deformation over the entire sphere allows us to consider self-gravitation effects naturally with less expensive computational costs than cases when using 3-D finite elements. It has been pointed out that computational methods based on a spherical harmonic development is subject to the problem of mode coupling when handling sharp lateral viscosity variations (Wu 2002, 2004). The weak formulation in the presented approach (Martinec 2000) partly suppresses the effect due to mode coupling because viscosity is prescribed as piecewise constant and usually taken as a value in the middle of a discretization interval in lateral direction. This acts as a certain type of filtering of high frequencies in lateral direction.

The paper is structured as follows. In a first step, we present the spectral-finite element representation in which the effect of compressibility is incorporated. The effect of compressibility is treated without an approximation. The representations are derived for 1-D and 3-D viscosity models. In order to keep the model comparable with results by alternative methods, we apply the presented method to a spherically symmetric model only and leave applications to a 3-D model for a further study. Moreover, we will not focus on resolving the problem of the instability modes, namely, the influence of these modes are included in computational results shown, as in other numerical approaches (e.g. Hanyk *et al.* 1999; Tanaka *et al.* 2009). In Section 2, we present the mandatory changes that have to be applied to the theory of Martinec (2000) and refer that for the complete expression of the theory. In Section 3, computational results obtained with the derived formulation are validated against the results obtained with independent methods. In Section 4, the global pattern of present-day global displacement rate due to postglacial rebounds is discussed by comparing forward modelling of compressible and incompressible earth models. Here, we emphasize the need for correcting the flexural rigidity of the elastic lithosphere.

2 FORMULATION

To avoid redundancy, during the presentation of the theoretical formulation, only the differences due to introducing compressibility are shown. For convenience, eq. (I-#) denotes eq. (#) in Martinec (2000).

2.1 Governing equations and boundary conditions

The momentum conservation and the Poissons's equation for viscoelastic deformation of an initially hydrostatically pre-stressed self-gravitating sphere are given as

$$\text{div}\boldsymbol{\tau} - \rho_0\text{grad}\phi_1 + \text{div}(\rho_0\mathbf{u})\text{grad}\phi_0 - \text{grad}(\rho_0\mathbf{u} \cdot \text{grad}\phi_0) = \mathbf{0}, \tag{1}$$

$$\nabla^2\phi_1 + 4\pi G\text{div}(\rho_0\mathbf{u}) = 0 \tag{2}$$

(e.g. Dahlen 1974) (the same as eqs I-1 and I-2), where $\mathbf{u}$, ϕ, $\boldsymbol{\tau}$ and G represent the displacement, the gravity potential increment, the stress tensor and Newton's gravitational constant, respectively, $\rho_0 = \rho_0(r)$ is the initial density, r is the radial distance from the centre of the Earth. The hydrostatic and the perturbed states are expressed by the subscripts 0 and 1, respectively. The constitutive equation for Maxwell rheology (Hanyk *et al.* 1995) can be represented as

$$\dot{\boldsymbol{\tau}} = \dot{\boldsymbol{\tau}}^E - \frac{\mu}{\eta}\left(\boldsymbol{\tau} - \frac{1}{3}\text{tr}\boldsymbol{\tau}\mathbf{I}\right), \tag{3}$$

$$\boldsymbol{\tau}^E = \lambda(\text{div}\mathbf{u})\mathbf{I} + 2\mu\boldsymbol{\epsilon}, \tag{4}$$

$$\boldsymbol{\epsilon} = \frac{1}{2}(\text{grad}\mathbf{u} + \text{grad}^{\text{T}}\mathbf{u}), \tag{5}$$

$$\frac{1}{3}\text{tr}\boldsymbol{\tau} = K\text{div}\mathbf{u} = \left(\lambda + \frac{2}{3}\mu\right)\text{div}\mathbf{u}, \tag{6}$$

where $\boldsymbol{\epsilon}$ represents the strain tensor and $\lambda = \lambda(r)$, $\mu = \mu(r)$, $K = K(r)$ and $\eta = \eta(\mathbf{r})$ are Lame's constants, the bulk modulus and the dynamic viscosity, respectively. The boundary conditions for surface loading are the same as in the incompressible case (eqs I-6–I-11). The deformation is solved for a spherical shell confined by the core–mantle boundary (CMB) and the Earth's surface.

In the incompressible case, the divergence-free constraint ($\text{div}\mathbf{u} = 0$) and the parametrization for the pressure increment ($\Pi = \lambda\text{div}\mathbf{u}$ as $\lambda \to \infty$ and $\text{div}\mathbf{u} \to 0$) are considered in addition to the above equations (e.g. Wu & Peltier 1982). As a result, $\frac{1}{3}\text{tr}\boldsymbol{\tau}$ in eq. (3) and $\lambda\text{div}\mathbf{u}$ in eq. (4) are replaced by Π (eqs I-3–I-5).

2.2 Time-differencing scheme

The time variation in the constitutive equation (eq. 3) is solved by applying an explicit Euler scheme of finite differences. Substituting eqs (4) and (6) into (3) yields

$$\boldsymbol{\tau}^{i+1} = \boldsymbol{\tau}^{E,i+1} + \boldsymbol{\tau}^{V,i}, \tag{7}$$

$$\boldsymbol{\tau}^{V,i} = (1 - M^i)\boldsymbol{\tau}^{V,i-1} - 2\mu M^i\boldsymbol{\epsilon}^i + \frac{2}{3}\mu M^i(\text{div}\mathbf{u}^i)\mathbf{I}, \tag{8}$$

$$\boldsymbol{\tau}^{V,0} = -2\mu M^0\boldsymbol{\epsilon}^0 + \frac{2}{3}\mu M^i(\text{div}\mathbf{u}^0)\mathbf{I}, \tag{9}$$

$$M^i = \frac{\mu}{\eta}(t^{i+1} - t^i), \tag{10}$$

where t^i denotes the time at the ith time step with $i = 0$ being the initial instant. The dilatational terms in eqs (8) and (9) appear when compressibility is considered (compare to eqs I-23–I-25).

2.3 Weak formulation and energy functional

In the weak formulation (Martinec 2000), the viscoelastic deformation is obtained which satisfies the variational equality at each time step. The latter consists of the energy functionals associated with elastic deformation, self-gravitation and uniqueness of the solution and the linear functionals associated with the viscous dissipation and the boundary conditions:

$$\delta\mathcal{E}(\mathbf{u}^{i+1}, \phi_1^{i+1}, \Pi^{i+1}, \delta\mathbf{u}, \delta\phi_1, \delta\Pi) = \delta\mathcal{E}_{\text{press}}(\mathbf{u}^{i+1}, \Pi^{i+1}, \delta\mathbf{u}, \delta\Pi) + \delta\mathcal{E}_{\text{shear}}(\mathbf{u}^{i+1}, \delta\mathbf{u})$$

$$+ \delta\mathcal{E}_{\text{grav}}(\mathbf{u}^{i+1}, \phi_1^{i+1}, \delta\mathbf{u}, \delta\phi_1) + \delta\mathcal{E}_{\text{uniq}}(\mathbf{u}^{i+1}, \delta\mathbf{u})$$

$$= \delta\mathcal{F}_{\text{diss}}^i(\delta\mathbf{u}) + \delta\mathcal{F}_{\text{surf}}^{i+1}(\delta\mathbf{u}, \delta\phi_1) \tag{11}$$

(eq. I-47). In the compressible case, energy functionals related to elastic deformation can be written as

$$\mathcal{E}^{\text{el}} = \frac{1}{2}\int_V (\boldsymbol{\tau}^{E,i+1} : \boldsymbol{\epsilon}^{i+1})\mathrm{d}V = \mathcal{E}_{\text{bulk}}(\mathbf{u}^{i+1}) + \mathcal{E}_{\text{shear}}(\mathbf{u}^{i+1}), \tag{12}$$

$$\mathcal{E}_{\text{bulk}} = \frac{1}{2}\int_V \lambda(\text{div}\mathbf{u}^{i+1})(\text{div}\mathbf{u}^{i+1})\mathrm{d}V, \tag{13}$$

$$\mathcal{E}_{\text{shear}} = \int_V \mu(\boldsymbol{\epsilon}^{i+1} : \boldsymbol{\epsilon}^{i+1}) dV, \tag{14}$$

where the form of $\mathcal{E}_{\text{shear}}$ is the same as for the incompressible case and the energy functional associated with the pressure, $\mathcal{E}_{\text{press}}$ is replaced by $\mathcal{E}_{\text{bulk}}$. The symbol: denotes the double-dot product of tensors. The variation of the bulk energy is written as

$$\delta\mathcal{E}_{\text{bulk}}(\mathbf{u}^{i+1}, \delta\mathbf{u}) = \int_V \lambda(\text{div}\mathbf{u}^{i+1})(\text{div}\delta\mathbf{u}) dV, \tag{15}$$

where $\delta\mathbf{u}$ denotes a test function (eq. I-55). The variation of the dissipation term on the right-hand side of the variational equality,

$$\delta\mathcal{F}_{\text{diss}}^i(\delta\mathbf{u}) = -\int_V (\boldsymbol{\tau}^{V,i} : \delta\boldsymbol{\epsilon}) dV \tag{16}$$

(eq. I-45), is also modified due to the addition of the dilatational term in eq. (8). Here, $\delta\boldsymbol{\epsilon}$ denotes the strain tensor evaluated for the test function (eq. I-104). Using the representations of eqs (15) and (16), it can be shown that all governing field equations and the boundary conditions are fulfilled by the variational equality for all test functions which are sufficiently smooth (Martinec 2000).

2.4 Spectral-finite element representation of the additional terms

The angular dependence of a solution ($\mathbf{u}, \phi_1$) and a test function ($\delta\mathbf{u}, \delta\phi_1$) is approximated by vector and scalar spherical harmonics (spectral representation):

$$\mathbf{u}(r, \theta, \varphi) = \sum_{j=0}^{\infty} \sum_{m=-j}^{j} \left[U_{jm}(r)\mathbf{S}_{jm}^{(-1)}(\theta, \varphi) + V_{jm}(r)\mathbf{S}_{jm}^{(1)}(\theta, \varphi) + W_{jm}(r)\mathbf{S}_{jm}^{(0)}(\theta, \varphi) \right],$$

$$\delta\mathbf{u}(r, \theta, \varphi) = \sum_{j=0}^{\infty} \sum_{m=-j}^{j} \left[\delta U_{jm}(r)\mathbf{S}_{jm}^{(-1)}(\theta, \varphi) + \delta V_{jm}(r)\mathbf{S}_{jm}^{(1)}(\theta, \varphi) + \delta W_{jm}(r)\mathbf{S}_{jm}^{(0)}(\theta, \varphi) \right],$$

$$\phi_1(r, \theta, \varphi) = \sum_{j=0}^{\infty} \sum_{m=-j}^{j} F_{jm}(r)Y_{jm}(\theta, \varphi),$$

$$\delta\phi_1(r, \theta, \varphi) = \sum_{j=0}^{\infty} \sum_{m=-j}^{j} \delta F_{jm}(r)Y_{jm}(\theta, \varphi), \tag{17}$$

where θ and φ are colatitude and longitude, respectively, U_{jm} and V_{jm} denote the coefficients of the vertical and horizontal displacements for the spheroidal component with degree j and order m and W_{jm} represents the toroidal component. The definition of these spherical harmonics is given in appendix of Martinec (2000). According to the previous section, modifications due to the introduction of compressibility are necessary only for $\delta\mathcal{E}_{\text{bulk}}$ and $\boldsymbol{\tau}^{V,i}$, which are now decomposed by the tensor spherical harmonics and the radial linear finite elements. The resulting parametrization of the variation of the bulk energy (eq. 15) can be written as

$$\text{div}\mathbf{u} = \sum_{jm} \left(\frac{dU_{jm}}{dr} + \frac{2U_{jm}}{r} - \frac{JV_{jm}}{r} \right) Y_{jm}(\theta, \varphi), \tag{18}$$

$$\text{div}\delta\mathbf{u} = \sum_{jm} \left(\frac{d\delta U_{jm}}{dr} + \frac{2\delta U_{jm}}{r} - \frac{J\delta V_{jm}}{r} \right) Y_{jm}(\theta, \varphi), \tag{19}$$

$$\delta\mathcal{E}_{\text{bulk}} = \sum_{jm} \int_b^a \lambda \left(\frac{dU_{jm}}{dr} + \frac{2U_{jm}}{r} - \frac{JV_{jm}}{r} \right) \left(\frac{d\delta U_{jm}^*}{dr} + \frac{2\delta U_{jm}^*}{r} - \frac{J\delta V_{jm}^*}{r} \right) r^2 dr, \tag{20}$$

where $J = j(j + 1)$, asterisk indicates complex conjugate, and a and b are the radii of the Earth's surface and the CMB, respectively. Applying the finite element parametrization by the piecewise linear base functions (eq. I-72) to the radial dependency of displacement and approximating the Lame's constant λ by piecewise constant functions, that is $\lambda(r) = \lambda_k$ for $r_k \leq r \leq r_{k+1}$ in a similar way as for $\mu(r)$ (eq. I-75), we obtain

$$\delta\mathcal{E}_{\text{bulk}} = \sum_{jm} \sum_{k=1}^{P} \lambda_k \sum_{\alpha=k}^{k+1} \sum_{\beta=k}^{k+1} \left[\left(I_{\alpha\beta}^{(1)} + 2I_{\alpha\beta}^{(3)} + 2I_{\beta\alpha}^{(3)} + 4I_{\alpha\beta}^{(6)} \right) U_{jm}^{\alpha} \delta U_{jm}^{\beta*} \right. \tag{21}$$

$$+ \left(-JI_{\beta\alpha}^{(3)} - 2JI_{\alpha\beta}^{(6)} \right) U_{jm}^{\alpha} \delta V_{jm}^{\beta*} \tag{22}$$

$$+ \left(-JI_{\alpha\beta}^{(3)} - 2JI_{\alpha\beta}^{(6)} \right) V_{jm}^{\alpha} \delta U_{jm}^{\beta*} \tag{23}$$

$$\left. + J^2 I_{\alpha\beta}^{(6)} V_{jm}^{\alpha} \delta V_{jm}^{\beta*} \right], \tag{24}$$

where k and P are the index of a layer in the radial direction and the number of subintervals between $r = b$ and a, respectively, and $I_{\alpha\beta}^{(1,3,4,6)}$ are given in appendix C of Martinec (2000).

The representations for the time variation of the viscous part of the stress (eq. 8) are derived differently for the 1-D and 3-D cases. For the 1-D case, $\tau^{V,i}$ is expanded in terms of the tensor spherical harmonics $\mathbf{Z}_{jm}^n$ (for the definition see appendix B of Martinec 2000) as

$$\tau^{V,i}(r, \Omega) = \sum_{jm} \sum_{n=1}^{6} \tau_{jm}^{V,i,n}(r) \mathbf{Z}_{jm}^n(\Omega). \tag{25}$$

The radial coefficients are approximated by finite elements as

$$\tau_{jm}^{V,i,n} = A_{k,jm}^{i,n} \frac{1}{h_k} + B_{k,jm}^{i,n} \frac{\psi_k(r)}{r} + C_{k,jm}^{i,n} \frac{\psi_{k+1}(r)}{r}, \tag{26}$$

where $h_k = r_{k+1} - r_k$ and ψ_k and ψ_{k+1} are the linear base functions for $r_k \le r \le r_{k+1}$ (eqs I-108–I-109). The strain is expressed according to eqs (I-85) and (I-86) as

$$\epsilon(r, \Omega) = \sum_{jm} \sum_{n=1}^{6} \epsilon_{jm}^n \mathbf{Z}_{jm}^n = \sum_{jm} \sum_{n=1}^{6} \left[\frac{a_{jm}^n}{h_k} + b_{jm}^n \frac{\psi_k(r)}{r} + c_{jm}^n \frac{\psi_{k+1}(r)}{r} \right] \mathbf{Z}_{jm}^n. \tag{27}$$

The dilatational term can be written as

$$(\mathrm{div}\mathbf{u}^i)\mathbf{I} = \sum_{jm} \left(\frac{\mathrm{d}U_{jm}^i}{\mathrm{d}r} + \frac{2U_{jm}^i}{r} - \frac{JV_{jm}^i}{r} \right) Y_{jm}(\mathbf{e}_{rr} + \mathbf{e}_{\theta\theta} + \mathbf{e}_{\varphi\varphi}) \tag{28}$$

$$= \sum_{jm} \left(\frac{\mathrm{d}U_{jm}^i}{\mathrm{d}r} + \frac{2U_{jm}^i}{r} - \frac{JV_{jm}^i}{r} \right) \left(\mathbf{Z}_{jm}^1 - \frac{1}{J} \mathbf{Z}_{jm}^5 \right), \tag{29}$$

where $\mathbf{e}_{rr}$, $\mathbf{e}_{\theta\theta}$ and $\mathbf{e}_{\varphi\varphi}$ are the dyadics of spherical base vectors (Martinec 2000, appendix B). Substituting eqs (25)–(29) into eq. (8), we have

$$\begin{bmatrix} A_{k,jm}^{i,n} \\ B_{k,jm}^{i,n} \\ C_{k,jm}^{i,n} \end{bmatrix} = \left(1 - M_k^i\right) \begin{bmatrix} A_{k,jm}^{i-1,n} \\ B_{k,jm}^{i-1,n} \\ C_{k,jm}^{i-1,n} \end{bmatrix} - 2\mu_k M_k^i \begin{bmatrix} a_{k,jm}^n(\mathbf{u}^i) \\ b_{k,jm}^n(\mathbf{u}^i) \\ c_{k,jm}^n(\mathbf{u}^i) \end{bmatrix}$$

$$+ \frac{2}{3} \mu_k M_k^i R^n \begin{bmatrix} a_{k,jm}'(\mathbf{u}^i) \\ b_{k,jm}'(\mathbf{u}^i) \\ c_{k,jm}'(\mathbf{u}^i) \end{bmatrix}, \tag{30}$$

$$\begin{bmatrix} a_{k,jm}'(\mathbf{u}^i) \\ b_{k,jm}'(\mathbf{u}^i) \\ c_{k,jm}'(\mathbf{u}^i) \end{bmatrix} = \begin{bmatrix} (U_{k+1,jm}^i - U_{k,jm}^i)/h_k \\ (2U_{k,jm}^i - JV_{k,jm}^i)/r \\ (2U_{k+1,jm}^i - JV_{k+1,jm}^i)/r \end{bmatrix}. \tag{31}$$

Here, $R^1 = 1$ and $R^5 = -1/J$. For $n = 2, 3, 4$ and 6, $R^n = 0$, that is, eq. (30) is exactly the same as for the incompressible case (eq. I-107). Eqs (30) and (31) give the time evolution of the viscous part of the stress tensor (eq. 26). Substituting eq. (26) into eq. (I-110), and using eqs (I-94) and (I-96), the variation of the dissipative energy at each time step is computed as

$$\int_V (\tau^{V,i} : \delta\epsilon)\mathrm{d}V = \sum_{k=1}^{P} \sum_{\alpha=1}^{2} \frac{r_\alpha^2 h_k}{2} \left[\int (\tau^{V,i} : \delta\epsilon)\mathrm{d}\theta\,\mathrm{d}\varphi \right]_{r=r_\alpha},$$

$$\int (\tau^{V,i} : \delta\epsilon)\mathrm{d}\theta\,\mathrm{d}\varphi = \sum_{jm} \left[\tau_{jm}^{V,i,1}(r)\delta\epsilon_{jm}^{1*}(r) + \frac{1}{2}J\tau_{jm}^{V,i,2}(r)\delta\epsilon_{jm}^{2*}(r) + \frac{1}{2}J\tau_{jm}^{V,i,3}(r)\delta\epsilon_{jm}^{3*}(r) \right.$$

$$\left. + \frac{1}{2}J(J-2)\tau_{jm}^{V,i,4}(r)\delta\epsilon_{jm}^{4*}(r) + 2J^2\tau_{jm}^{V,i,5}(r)\delta\epsilon_{jm}^{5*}(r) + 2J(J-2)\tau_{jm}^{V,i,6}(r)\delta\epsilon_{jm}^{6*}(r) \right], \tag{32}$$

where $r_\alpha = \frac{1}{2}(h_k x_\alpha + r_k + r_{k+1})$ and $x_{1,2} = \pm 1/\sqrt{3}$ and the orthogonality properties are used in the integration over angular variables.

For the 3-D case, the corresponding time evolution formula is reformulated for computational convenience. The strain tensor is represented in terms of the six symmetric spherical dyadics, that is, rr, $r\,\theta$, $r\,\varphi$, $\theta\,\theta$, $\theta\,\varphi$ and $\varphi\,\varphi$ components (eqs I-90–I-92), instead of using the coefficients of the orthogonal tensor spherical harmonics as in eq. (25). Accordingly, the viscous part of the stress is expressed by the six components of the dyadics (eq. I-103). Moreover, the angular dependence of strain and stress is numerically evaluated at gridpoints $\Omega_l = (\theta_l, \varphi_l)$ (eq. I-99). This is necessary because the viscosity is now laterally variable and becomes a function of Ω_l. Approximating the stress over a radial interval of $r_k \le r \le r_{k+1}$ as

$$\tau_{jm}^{V,i}(r, \Omega_l) = \mathbf{A}_{k,jm}^i(r, \Omega_l) \frac{1}{h_k} + \mathbf{B}_{k,jm}^{i,n}(r, \Omega_l) \frac{\psi_k(r)}{r} + \mathbf{C}_{k,jm}^{i,n}(r, \Omega_l) \frac{\psi_{k+1}(r)}{r}, \tag{33}$$

its time evolution (eq. 8) can be written as

$$
\begin{bmatrix}
\mathbf{A}^i_{k,jm}(\Omega_l) \\
\mathbf{B}^i_{k,jm}(\Omega_l) \\
\mathbf{C}^i_{k,jm}(\Omega_l)
\end{bmatrix}
= (1 - M^i_{kl})
\begin{bmatrix}
\mathbf{A}^{i-1}_{k,jm}(\Omega_l) \\
\mathbf{B}^{i-1}_{k,jm}(\Omega_l) \\
\mathbf{C}^{i-1}_{k,jm}(\Omega_l)
\end{bmatrix}
- 2\mu_k M^i_{kl}
\begin{bmatrix}
\mathbf{a}_{k,jm}(\Omega_l;\mathbf{u}^i) \\
\mathbf{b}_{k,jm}(\Omega_l;\mathbf{u}^i) \\
\mathbf{c}_{k,jm}(\Omega_l;\mathbf{u}^i)
\end{bmatrix}
$$

$$
+ \frac{2}{3}\mu_k M^i_{kl}
\begin{bmatrix}
\mathbf{a}'_{k,jm}(\Omega_l;\mathbf{u}^i) \\
\mathbf{b}'_{k,jm}(\Omega_l;\mathbf{u}^i) \\
\mathbf{c}'_{k,jm}(\Omega_l;\mathbf{u}^i)
\end{bmatrix},
\tag{34}
$$

where

$$
\begin{bmatrix}
\mathbf{a}'_{k,jm}(\Omega_l;\mathbf{u}^i) \\
\mathbf{b}'_{k,jm}(\Omega_l;\mathbf{u}^i) \\
\mathbf{c}'_{k,jm}(\Omega_l;\mathbf{u}^i)
\end{bmatrix}
=
\begin{bmatrix}
(U^i_{k+1,jm} - U^i_{k,jm})/h_k \\
(2U^i_{k,jm} - JV^i_{k,jm})/r \\
(2U^i_{k+1,jm} - JV^i_{k+1,jm})/r
\end{bmatrix}
Y_{jm}(\Omega_l)(\mathbf{e}_{rr} + \mathbf{e}_{\theta\theta} + \mathbf{e}_{\varphi\varphi})
\tag{35}
$$

and

$$
M^i_{kl} = \frac{\mu_k}{\eta_{kl}}(t^{i+1} - t^i).
\tag{36}
$$

The variation of the dissipative energy (eq. 32) is computed as

$$
\int_V (\boldsymbol{\tau}^{V,i} : \delta\boldsymbol{\epsilon})\mathrm{d}V \approx \sum_{k=1}^{P}\sum_{\alpha=1}^{2} \frac{r_\alpha^2 h_k}{2} \sum_{l=1}^{L} w_l \Big[\boldsymbol{\tau}(r,\Omega_l)^{V,i} : \delta\boldsymbol{\epsilon}(r,\Omega_l)\Big]_{r=r_\alpha},
\tag{37}
$$

where w_l are weight factors and L is the total number of 2-D gridpoints (eq. I-97). The double-dot product on the right-hand side of eq. (37) is represented for $r_k \le r \le r_{k+1}$ as (eq. I-103)

$$
\boldsymbol{\tau}(r,\Omega)^{V,i} : \delta\boldsymbol{\epsilon}(r,\Omega) = \frac{1}{h_k} A^i_{k,rr}(\Omega) \sum_{jm} \big[\delta\epsilon^1_{jm}(r)Y_{jm}(\Omega)\big]^*
$$

$$
+ \frac{1}{2}\bigg[A^i_{k,r\theta}(\Omega)\frac{1}{h_k} + B^i_{k,r\theta}(\Omega)\frac{\psi_k(r)}{r} + C^i_{k,r\theta}(\Omega)\frac{\psi_{k+1}(r)}{r}\bigg] \sum_{jm}\big[\delta\epsilon^2_{jm}(r)E_{jm}(\Omega) - \delta\epsilon^3_{jm}(r)F_{jm}(\Omega)\big]^*
$$

$$
+ \frac{1}{2}\bigg[A^i_{k,r\varphi}(\Omega)\frac{1}{h_k} + B^i_{k,r\varphi}(\Omega)\frac{\psi_k(r)}{r} + C^i_{k,r\varphi}(\Omega)\frac{\psi_{k+1}(r)}{r}\bigg] \sum_{jm}\big[\delta\epsilon^2_{jm}(r)F_{jm}(\Omega) + \delta\epsilon^3_{jm}(r)E_{jm}(\Omega)\big]^*
$$

$$
+ \bigg[B^i_{k,\theta\theta}(\Omega)\frac{\psi_k(r)}{r} + C^i_{k,\theta\theta}(\Omega)\frac{\psi_{k+1}(r)}{r}\bigg] \sum_{jm}\big[-\delta\epsilon^4_{jm}(r)H_{jm}(\Omega) - J\delta\epsilon^5_{jm}(r)Y_{jm}(\Omega) + \delta\epsilon^6_{jm}(r)G_{jm}(\Omega)\big]^*
$$

$$
+ \frac{1}{2}\bigg[B^i_{k,\theta\varphi}(\Omega)\frac{\psi_k(r)}{r} + C^i_{k,\theta\varphi}(\Omega)\frac{\psi_{k+1}(r)}{r}\bigg] \sum_{jm}\big[\delta\epsilon^4_{jm}(r)G_{jm}(\Omega) + 4\delta\epsilon^6_{jm}(r)H_{jm}(\Omega)\big]^*
$$

$$
+ \bigg[B^i_{k,\varphi\varphi}(\Omega)\frac{\psi_k(r)}{r} + C^i_{k,\varphi\varphi}(\Omega)\frac{\psi_{k+1}(r)}{r}\bigg] \sum_{jm}\big[\delta\epsilon^4_{jm}(r)H_{jm}(\Omega) - J\delta\epsilon^5_{jm}(r)Y_{jm}(\Omega) - \delta\epsilon^6_{jm}(r)G_{jm}(\Omega)\big]^*,
\tag{38}
$$

where the functions $E_{jm}(\Omega)$, $F_{jm}(\Omega)$, $G_{jm}(\Omega)$ and $H_{jm}(\Omega)$ are given in appendix B of Martinec (2000). In the compressible case, the last term in eq. (34) is added. Therefore, substituting eqs (33)–(36) into eq. (38), the following additional terms, compared to the incompressible case, appear on the right-hand side,

$$
\bigg[\frac{1}{h_k}a'^i_{k,jm,rr}(\Omega) + b'^i_{k,jm,rr}(\Omega)\frac{\psi_k}{r} + c'^i_{k,rr,jm}(\Omega)\frac{\psi_{k+1}}{r}\bigg] \sum_{jm}[\delta\epsilon^1_{jm}(r)Y_{jm}(\Omega)]^*
$$

$$
+ \bigg[\frac{1}{h_k}a'^i_{k,jm,\theta\theta}(\Omega) + b'^i_{k,jm,\theta\theta}(\Omega)\frac{\psi_k}{r} + c'^i_{k,jm,\theta\theta}(\Omega)\frac{\psi_{k+1}}{r}\bigg]
$$

$$
\times \sum_{jm}\big[-\delta\epsilon^4_{jm}(r)H_{jm}(\Omega) - J\delta\epsilon^5_{jm}Y_{jm}(\Omega) + \delta\epsilon^6_{jm}G_{jm}(\Omega)\big]^*
$$

$$
+ \bigg[\frac{1}{h_k}a'^i_{k,jm,\varphi\varphi}(\Omega) + b'^i_{k,jm,\varphi\varphi}(\Omega)\frac{\psi_k}{r} + c'^i_{k,jm,\varphi\varphi}(\Omega)\frac{\psi_{k+1}}{r}\bigg]
$$

$$
\times \sum_{jm}\big[\delta\epsilon^4_{jm}(r)H_{jm}(\Omega) - J\delta\epsilon^5_{jm}Y_{jm}(\Omega) - \delta\epsilon^6_{jm}G_{jm}(\Omega)\big]^*,
\tag{39}
$$

where

$$
a'^i_{k,jm,rr}(\Omega) = a'^i_{k,jm,\theta\theta}(\Omega) = a'^i_{k,jm,\varphi\varphi}(\Omega) = (U^i_{k+1,jm} - U^i_{k,jm})Y_{jm}(\Omega),
$$

$$
b'^i_{k,jm,rr}(\Omega) = b'^i_{k,jm,\theta\theta}(\Omega) = b'^i_{k,jm,\varphi\varphi}(\Omega) = (2U^i_{k,jm} - JV^i_{k,jm})Y_{jm}(\Omega),
$$

$$
c'^i_{k,jm,rr}(\Omega) = c'^i_{k,jm,\theta\theta}(\Omega) = c'^i_{k,jm,\varphi\varphi}(\Omega) = (2U^i_{k+1,jm} - JV^i_{k+1,jm})Y_{jm}(\Omega).
\tag{40}
$$

Table 1. A comparison of calculated elastic load Love numbers for a homogeneous earth model to analytical solutions from Wu & Peltier (1982).

j	Type	Analytic sol.	This study	Per cent diff.
2	h	−5.818E−01	−5.818E−01	0.01
	l	−1.218E−02	−1.218E−02	0.06
	k	−2.202E−01	−2.201E−01	0.01
10	h	−8.816E−01	−8.815E−01	0.01
	l	1.468E−02	1.468E−02	0.01
	k	−9.183E−02	−9.182E−02	0.01
60	h	−9.965E−01	−9.964E−01	0.01
	l	3.583E−03	3.583E−03	0.01
	k	−1.891E−02	−1.891E−02	0.00
100	h	−1.007E+00	−1.007E+00	0.01
	l	2.213E−03	2.213E−03	0.01
	k	−1.156E−02	−1.157E−02	0.03

Eqs (39) and (40) are the final expression used to compute the variation of the additional term occurring in dissipative energy that is due to considering compressibility for the 3-D case. The numerical computation algorithms for the volume integral of the dissipative energy and the Galerkin matrix are described in sections 8 and 10 of Martinec (2000).

3 VALIDATION

To validate the presented formulation, numerical results are compared with those obtained by independent methods (Wu & Peltier 1982; Tanaka *et al.* 2006, 2009). These methods are based on the same governing equations as described in Section 2. Since we restrict applications of the presented approach to 1-D models, comparisons are carried out for spherically symmetric earth models (Sections 3.1 and 3.2). Moreover, a stability of the employed computational scheme in a numerical aspect is discussed in Section 3.3.

3.1 Elastic deformation

First, elastic deformation is confirmed. A representation of the analytical solution for a homogeneous compressible earth model is listed in Wu & Peltier (1982). Table 1 shows a comparison between the load Love numbers for selected spherical harmonic degrees calculated by the analytical solution and those computed by the presented method. The load Love number is defined as $h_j(t = 0) = (M_e/a)U_{j0}(r = a, t = 0)$, $l_j(t = 0) = (M_e/a)V_{j0}(r = a, t = 0)$ and $k_j(t = 0) = -(M_e/ag_0)F_{j0}(r = a, t = 0)$, where M_e and g_0 denote the mass of the Earth and the surface gravity, respectively, and the earth model parameters are shown in table 1 of Wu & Peltier (1982). The load is Heaviside loading. The comparison shows that deviations between the both methods are less than 0.1 per cent. The differences decrease with increasing number of finite elements in the radial direction. This result indicates that the formulation of the bulk energy (eq. 20) is correct.

In Wu & Peltier (1982), a time-series of load Love number derived from the analytical solution is plotted for the homogeneous earth model. In this plot, the instability modes mentioned in Hanyk *et al.* (1999) are excluded when eigenmodes are searched by the normal mode method. On the other hand, the effect of instability modes appears in our result after some time as shown by Hanyk *et al.* (1999), which uses the time-domain approach. Therefore, transient deformation is not fully comparable with the analytical solution.

3.2 Viscoelastic deformation

To confirm that transient deformation is computed correctly, we use a numerical inverse Laplace integration method (Tanaka *et al.* 2006, 2009). Several compressible earth models have been employed for this validation, namely, homogeneous model, two-layer model, PREM (Dziewonski & Anderson 1981) averaged on five/30 layers with/without a liquid core. In each layer of these models, the material property is uniform. The agreements between the load Love numbers ($h_j(t)$, $l_j(t)$, $k_j(t)$) calculated with both the methods are better than 2 per cent in general. For earth models where the instability (Hanyk *et al.* 1999; Vermeersen & Mitrovica 2000) occurs in a relatively short timescale, however, an agreement can only be seen up to the time prior to a growth of unstable modes becomes remarkable (e.g. up to 10 000 yr for a homogeneous earth model). This is an acceptable fact because numerical errors associated with the mode instability increase in a different manner for the two different algorithms. For a realistic model, it is known that unstable modes appear in longer timescales than geological ones (Vermeersen & Mitrovica 2000). As an example, Figs 1–3 show the load Love numbers computed for the PREM averaged on thirty layers with a liquid core, up to 1 Myr after the surface load is applied. The viscosity is 10^{30} Pa s within the lithosphere down to the depth of 45 km and 10^{21} Pa s from depths 45 km to CMB. The radial intervals of the earth model used for the finite element parametrization are 1–2 km in the lithosphere, 5–10 km in the upper mantle and 20 km in the lower mantle. The time step Δt is 100 yr. The 3-D formulation (eqs 26–30) is used for the computation of the dissipative energy and the numerical results are compared with the 1-D formulation (eqs 23–25). The differences are less than 1–2 per cent, which is caused by a numerical integration error over the angular variable Ω in the computation of
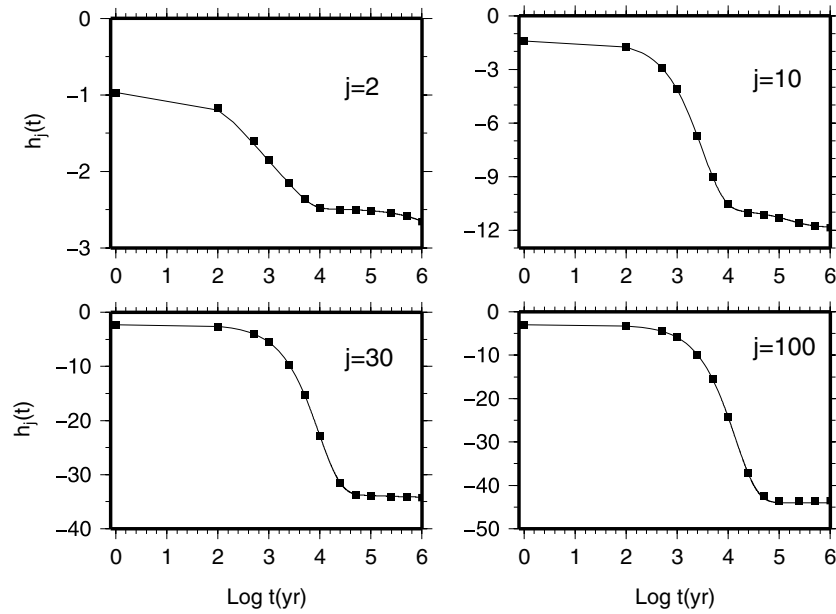
Figure 1. Comparison of the viscoelastic load Love number $h_j(t)$ for vertical displacement for different spherical harmonic degrees j. The horizontal axis indicates the time since the Heaviside-type surface load is applied at $t = 0$. The solid lines show the result obtained by the method presented in this study for a 1-D viscosity model. The squares display the results computed by the numerical Laplace integration method for the same model (Tanaka *et al.* 2009). The elastic earth model PREM is employed with the lithospheric thickness 45 km and the asthenospheric viscosity 10^{21} Pa s.
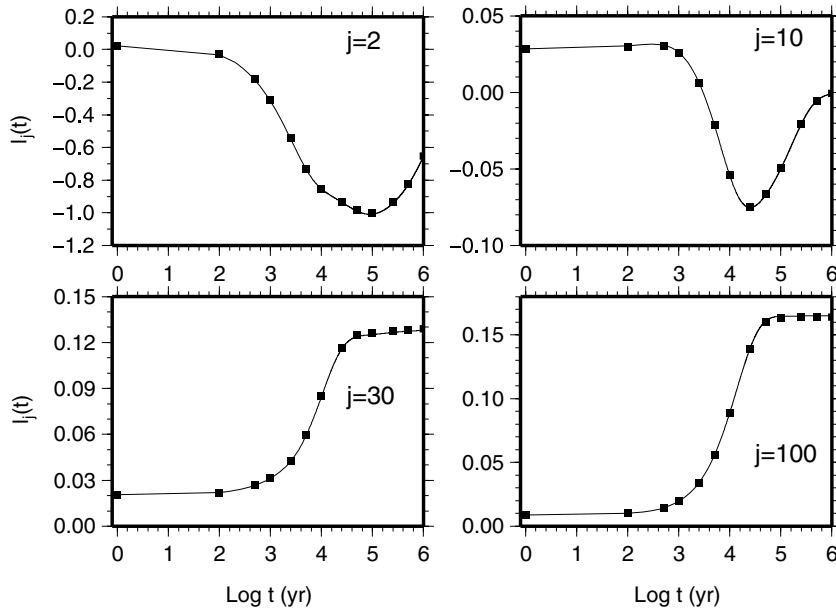
Figure 2. The same as Fig. 1 but for the load Love number $l_j(t)$ for horizontal displacement.

the dissipative energy. On the other hand, the method of Tanaka *et al.* (2009) can cause a numerical error of a few per cent in the calculation of the load Love numbers according to a choice of an integration path in the Laplace domain (Tanaka *et al.* 2007). Considering these facts, the results computed by the two different algorithms agree acceptably well, indicating that the formulation derived to include the effects of compressibility is correct.

3.3 A stability of a numerical computation at longer time period

For times greater than the Maxwell time, the response of viscoelastic material changes from elastic to fluid behaviour. In the normal mode approach, the fundamental matrix describing the differential equation reduces its form from a 6 × 6 matrix to a 2 × 2 matrix at the fluid limit (Wu & Peltier 1982). When a solution of the 6 × 6 set of equation approaches that of the 2 × 2 set of equation, the differential
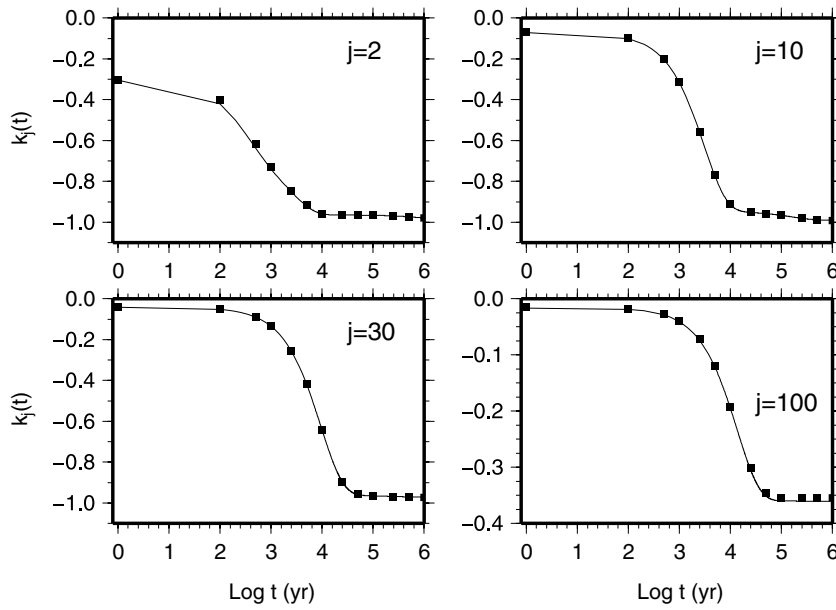
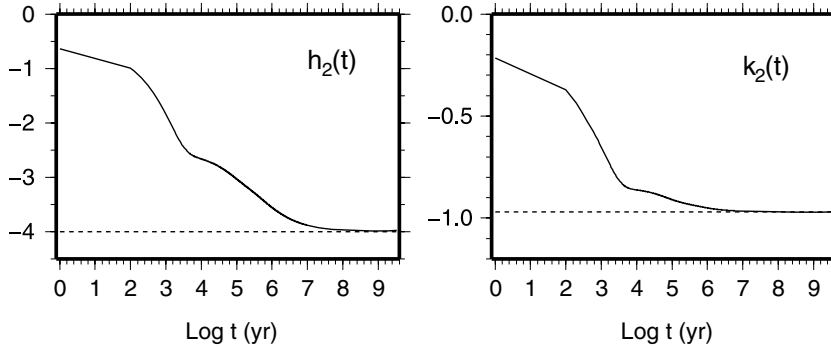**Figure 3.** The same as Fig. 1 but for the load Love number $k_j(t)$ for gravitational potential change.

Figure 4. The degree-two load Love numbers for a compressible earth model in which the density profile is artificially adjusted such that instability modes vanish (the solid line). For a longer time period, the load Love numbers agree with those computed for an earth model in which the rigidity below the lithosphere is set to zero. This shows that the computational scheme is numerically stable for computations at longer time periods when the mantle behaves like a liquid.

equation becomes stiff and a numerical instability arises which causes that the near fluid displacement oscillates. This problem becomes especially severe when compressibility is included.

In our computational results, such an instability is not seen. Fig. 4 shows the load Love numbers for a compressible PREM in which a density gradient is added such that the Adams–Williamson condition is satisfied. This modification allows us to distinguish a numerical instability from the physical instability. We see from the figure that the load Love numbers converge to the isostatic load Love numbers (Wu & Peltier 1982) computed for an earth model in which the rigidity below the lithosphere is replaced by zero. This indicates that the employed formulation remains stable for computations at longer time periods. The form of the fundamental matrix on the left-hand side of eq. (11) is constant in time and the dissipation term on the right-hand side, which is numerically evaluated, becomes smaller at longer time periods and finally vanishes.

4 APPLICATION TO THE GIA PROCESS

In this section, we apply the presented method to modelling of GIA. As an example, we model the present-day deformation rates induced by ICE5G/VM2 earth model/glaciation-history combination (Peltier 2004) together with the sea level equation of Hagedoorn *et al.* (2006). The influence of compressibility is investigated by comparing the result for a compressible earth model based on PREM, model C, with two incompressible models.

The first one, model IA, is PREM with setting the Lamé parameter $\lambda \to \infty$ (Wu & Peltier 1982), corresponding to a Poisson's ratio $\nu_{inc} = 0.5$. Therefore, the elastic rigidity, μ_{inc}, is not changed. The second one, model IB, is also PREM with $\lambda \to \infty$ but the elastic rigidity is adjusted such that the flexural rigidity, D_e (McConnell 1965; Walcott 1970), becomes the same as that of the compressible PREM. The
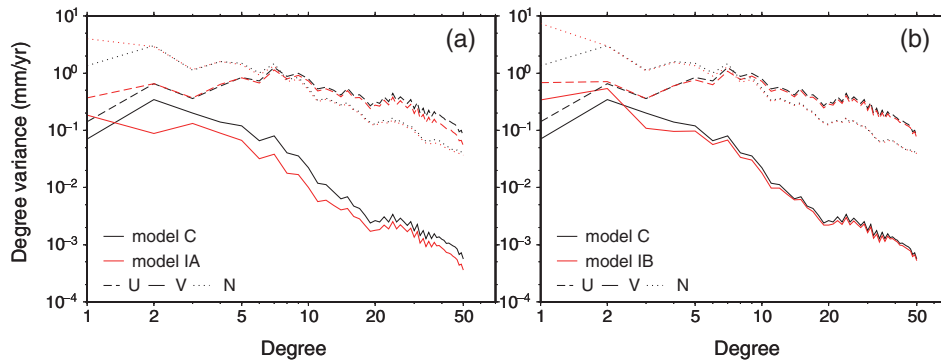
Figure 5. Comparisons between the degree variances of surface motion, horizontal component, V (solid), radial component, U (dashed) and of radial geoid displacement and N (dotted). The results are shown for a compressible model C and incompressible models IA and IB. In model IB, the flexural rigidity is adjusted.

elastic rigidity can be obtained from the following scaling law (Lambeck & Nakiboglu 1980)

$$\frac{dD_e}{dr} = \frac{2\mu(r)L^2}{1-\nu(r)} = \frac{2\mu_{inc}(r)L^2}{1-\nu_{inc}(r)}, \tag{41}$$

where μ and ν are the elastic rigidity and Poisson's ratio of the compressible model and $\nu_{inc} = 0.5$. The thickness of the elastic lithosphere, L, is the same for the three models. By this, a physically equivalent relaxation process is simulated in the presence of an elastic lithosphere. This treatment is also used in the comparison between the compressible and incompressible models in Tanaka *et al.* (2009).

4.1 Comparison with the incompressible model without the flexural rigidity adjusted

Fig. 5 shows a comparison between the degree variances of the present-day surface motion (see Klemann *et al.* 2008). Because of the spherically symmetric Earth structure employed, the toroidal displacement, W_{jm}, is not induced for the three earth models. The influence on the vertical displacement and the geoid is almost negligible if we disregard the components of degree 1, where the deviations are larger. This finding corresponds to the fact that compressibility of the Earth can be neglected for the modelling of vertical uplift and sea level change. In contrast, the horizontal velocities are markedly enhanced for the model C implying that the horizontal deformation is driven to a large extent by shear deformation.

The above tendency is also seen in the load Love number (Fig. 6) where the horizontal displacement evolves differently for the compressible and incompressible models. For the vertical displacement, the elastic response is larger for model C, which is consistent with the result of Wolf (1985). This indicates that the influence of compressibility on the vertical component of GIA is small as long as no present time loading is considered where the elastic component of displacement appears. For $j = 1$, the deformation refers to the centre of mass of the Earth plus load (CM) (Klemann & Martinec 2009). Note that some studies refer to the centre of mass of the undeformed Earth (e.g. Farrell 1972; Saito 1974; Okubo & Endo 1986).

If we compare the deformation patterns in the spatial domain (Figs 7a and b), we observe a more symmetric pattern around the regions of former glaciation for model C than for model IA, visible as red spots marking the maxima of postglacial uplift. The horizontal rates are enhanced approximately by a factor of two for model C when compared with model IA. Furthermore, the horizontal displacement rates decrease much faster with distance from these regions. This feature indicates more localized mass redistributions around the load due to compressibility and so less dynamic interaction between the GIA in Laurentide and Fennoscandia.

4.2 Comparison with the incompressible model with the flexural rigidity adjusted

In this comparison, the elastic rigidity within the lithosphere [i.e. $\mu(r)$ for $r \geq 6281$ km] is parametrized for the incompressible model IB as

$$\mu^{inc}(r) = \mu(r)\frac{\lambda(r) + \mu(r)}{\lambda(r) + 2\mu(r)} \tag{42}$$

(see eq. 41). From Fig. 5(b) showing the degree variances of models C and IB, we see that the difference in the vertical components (Fig. 5a) between model IA and C for $j > 20$ almost disappears. In the horizontal component, the fit between model IB and C is quite well for shorter wavelengths, whereas the difference is not completely removed for longer wavelengths ($j < 5$). In particular, the horizontal displacement rate for model IB for degree $j = 2$ becomes larger than that for model C, although the difference between them is smaller than the difference between models C and IA (Fig. 5a). At degree 1, no agreement is seen between model IA, IB and C.

A similar tendency is seen if the load Love numbers are compared (Fig. 6). The comparison of the vertical displacements of lower degrees ($j \leq 10$) for model IA and IB shows that vertical deformation for such degrees is not affected by the adjustment of the flexural rigidity. The reason why the degree variances for $j = 1$ differ between IA and IB (Figs 5a and b) in spite of the agreement in the load Love
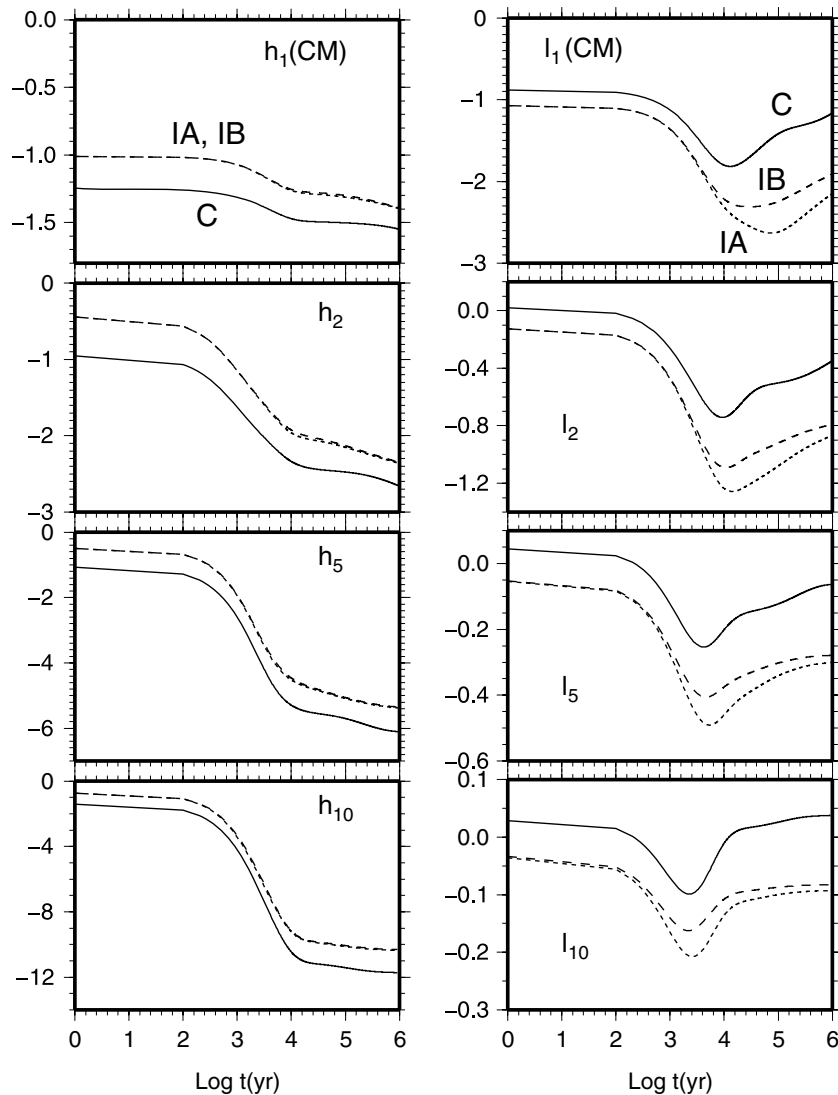
Figure 6. The effects of compressibility on the lower-degree load Love numbers $h_j(t)$ and $l_j(t)$. Solid, dotted and dashed lines, respectively denote the results for the compressible model C and the incompressible models IA and IB. In model IB, the flexural rigidity is adjusted. For $j = 1$, centre of mass of the whole Earth (CM) is chosen as the origin of the reference frame (Klemann & Martinec 2009).

numbers is that the degree variance of $j = 1$ includes the effect of the realization of the reference frame in addition to the response to the load (Klemann & Martinec 2009). In the horizontal displacement, differences between the compressible model C and the incompressible model IB with the adjusted flexural rigidity decrease after $t > 1$ kyr by approximately 30 per cent.

Fig. 7(c) shows the velocity field in the spatial domain for model IB. Compared to model IA and C, we see that the far-field horizontal displacement rate increases for model IB, indicating that the adjustment of the flexural rigidity does not necessarily reduce the difference from the compressible model in the spatial domain for lower degrees. Further detail can be gained by plotting the differences in velocity fields. In Figs 8(a) and (b), the differences between models C and IA and those between models C and IB are plotted, respectively. In Figs 8(c) and (d), the differences in deformation rate are shown only for degrees larger than 5. These figures confirm that the reduction of the difference for higher degrees is better achieved when using a model with the adjusted flexural rigidity. In contrast, when considering also Figs 8(a) and (b), it becomes quite visible that the differences in the velocity fields are dominated by the low degrees. The difference between models C and IB for $j = 2$ (Fig. 8b) is dominating the plotted difference field and is larger than for C–IA (Fig. 8a). This shows that the low degree response is dominated by a process which is not parametrized by the flexural rigidity.

We can resume these findings as follows. (i) If the incompressible PREM is used without adjustment of the flexural rigidity of the lithosphere, a large difference between the compressible and incompressible models is seen in the present-day horizontal displacement rates which amount to 1–2 mm yr^{-1} around the regions of the former glaciation, and which are detectable with GPS. (ii) By adjusting the flexural rigidity, the difference from the compressible model almost disappears. However, for longer wavelengths ($j < 5$), the difference still remains at 1 mm yr^{-1} on a global scale.

Present–day velocity:

— 3 mm/yr

−10   0   10

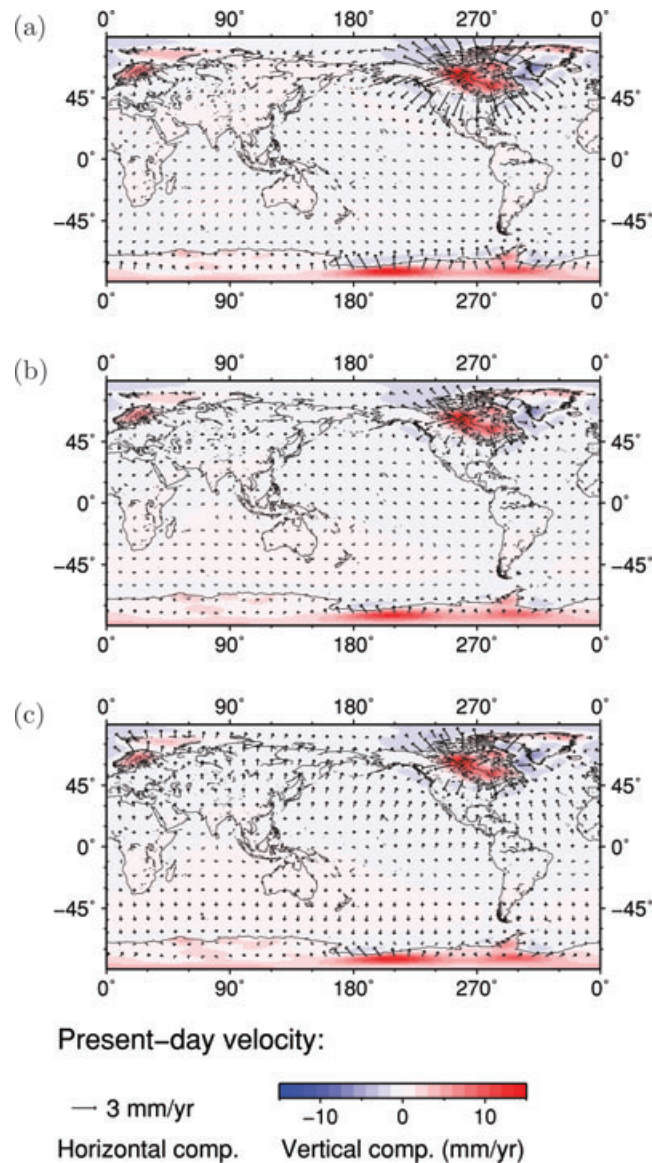Horizontal comp.   Vertical comp. (mm/yr)

Figure 7. Present-day surface velocities for (a) the compressible model C, (b) the incompressible model IA and (c) the incompressible model IB with the flexural rigidity adjusted.

5 CONCLUSION

The spectral-finite element approach to viscoelastic relaxation induced by surface loading outlined in Martinec (2000) has been extended to the case of compressibility. The correctness of the presented solutions is confirmed by the comparison with results obtained by independent computation methods for the same model setting (Wu & Peltier 1982; Tanaka *et al.* 2009). The presented method may serve as one of the methods to incorporate the effect of compressibility, which has been often neglected in the modelling of GIA. In addition, the method allows us to consider the effect of self-gravitation and large-scale lateral heterogeneities in viscosity.

As an example, we modelled the present-day deformation rate using Peltier (2004)'s ICE5G/VM2 earth-model/glaciation-history combination together with the sea level equation of Hagedoorn *et al.* (2006). To elucidate the influence of compressibility on the present-day velocity field, we compared the results obtained by compressible and incompressible models. In the presence of compressibility, the horizontal deformation rate is roughly twice as large around Laurentide and Fennoscandia and decreases with distance from these regions faster, compared to the incompressible model. This indicates a more constrained mass redistribution inside the mantle due to compressibility and so less dynamic interaction between the GIA in Laurentide and Fennoscandia. In contrast, the vertical displacement rate is only slightly affected by compressibility. The difference in the horizontal rate amounts to 1–2 mm yr^{-1}, which is detectable by GPS. Therefore, the consideration of compressibility is mandatory in the modelling of GIA. The differences between the compressible and incompressible models are reduced below a detectable level for shorter wavelengths, by adjusting the elastic rigidity in the incompressible model so that the flexural rigidity
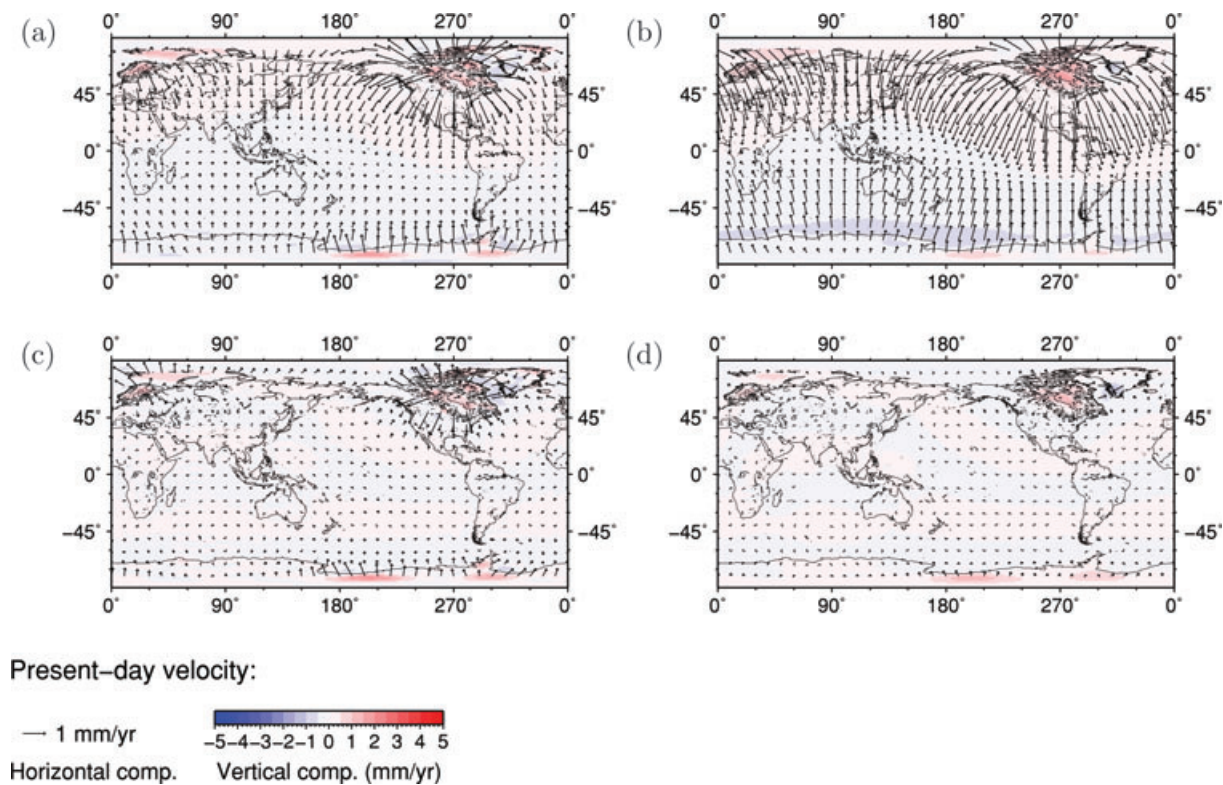
Figure 8. Differences between the velocity fields for (a) the compressible model minus the incompressible model (C–IA), (b) the compressible model minus the incompressible model with the flexural rigidity adjusted (C–IB). (c, d) are the same as (a, b) but only spherical harmonic degrees $j > 5$ are considered. The scaling is amplified by a factor of 3 with respect to Fig. 7.

becomes the same. However, the difference of 1 mm yr^{-1} still remains on a global scale. Therefore, if discussing a global motion induced by GIA, the influence of compressibility should be considered.

ACKNOWLEDGMENTS

REFERENCES

Beutler, G., Drewes, H. & Verdun, A., 2005. The Integrated Global Geodetic Observing System (IGGOS) viewed from the perspective of history, *J. Geodyn., **40,** 414–431.

Cambiotti, G. & Sabadini, R., 2009. The compressional and compositional stratifications in Maxwell earth models: the gravitational overturning and the long-period tangential flux, *Geophys. J. Int.,* **180,** 475–500.

Chaljub, E., Capdeville, Y. & Vilotte, J.P., 2003. Solving elastodynamics in a fluid solid heterogeneous sphere: a parallel Spectral Element approximation on non-conforming grids, *J. Comp. Phys.,* **187**(2) 457–491.

Dahlen, F.A., 1974. On the static deformation of an Earth model with a fluid core, *Geophys. J. R. astr. Soc.,* **36,** 461–485.

Dziewonski, A.M. & Anderson, A., 1981. Preliminary reference earth model, *Phys. Earth planet. Inter.,* **25,** 297–356.

Farrell, W.E., 1972. Deformation of the Earth by Surface Loads, *Rev. Geophys.,* **10**(3), 761–797.

Hagedoorn, J.M., Wolf, D. & Martinec, Z., 2006. An estimate of global sea level rise inferred form tide gauge measurements using glacial isostatic models consistent with the relative sea level record, *Pure appl. Geophys.,* **164,** 791–818.

Han, D. & Wahr, J., 1995. The viscoelastic relaxation of a realistically stratified Earth, and a further analysis of postglacial rebound, *Geophys. J. Int.* **120,** 287–311.

Hanyk, L., Moser, J., Yuen, D.A. & Matyska, C., 1995. Time-domain approch for the transient responses in stratified viscoelastic Earth models, *Geophys. Res. Lett.,* **22,** 1285–1288.

Hanyk, L., Matyska, C. & Yuen, D.A., 1998. Initial-value approach for viscoelastic responses of the Earth's mantle, in *Dynamics of the Ice Age Earth: A Modern Perspective,* pp. 135–154, ed. Wu, P., Trans Tech Publications, Hetikon.

Hanyk, L., Matyska, C. & Yuen, D.A., 1999. Secular gravitational instability of a compressible viscoelastic sphere, *Geophys. Res. Lett.,* **26,** 557–560.

Karato, S., 2003. *The Dynamic Structure of the Deep Earth, An Interdisciplinary Approach,* 264 pp., Princeton Univ. Press, NJ.

Kaufmann, G. & Wu, P., 1998. Lateral asthenospheric viscosity variations and postglacial rebound: a case study for the Barents Sea, *Geophys. Res. Lett.,* **25,** 1963–1966.

Kaufmann, G. & Wolf, D., 1999. Effects of lateral viscosity variations on postglacial rebound: an analytical approach, *Geophys. J. Int.,* **137,** 489–500.

Kaufmann, G. & Wu, P., 2002. Glacial isostatic adjustment in Fennoscandia with a three-dimensional viscosity structure as an inverse problem, *Earth planet. Sci. Lett.,* **197,** 1–10.

Kaufmann, G., Wu, P. & Wolf, D., 1997. Some efects of lateral heterogeneities in the upper mantle on postglacial land uplift close to continental margins, *Geophys. J. Int.,* **127,** 175–187.

Kaufmann, G., Wu, P. & Ivins, E.R., 2005. Lateral viscosity variations beneath Antarctica and their implications on regional rebound motions and seismotectonics, *J. Geodyn.,* **39,** 165–181.

Klemann, V. & Martinec, Z., 2009. Contribution of glacial-isostatic adjustment to the geocenter motion, *Tectonophys,* doi:10.1016/ j.tecto.2009.08.031.

Klemann, V., Wu, P. & Wolf, D., 2003. Compressible viscoelasticity: stability of solutions for homogeneous plane-Earth models, *Geophys. J. Int.,* **153,** 569–585.

Klemann, V., Ivins, E.R., Martinec, Z. & Wolf, D., 2007. Models of active glacial isostasy roofing warm subduction: case of the South Patagonian Ice Field, *J. geophys. Res.,* **112,** B09405, doi:10.1029/2006JB004818.

Klemann, V., Martinec, Z. & Ivins, E.R., 2008. Glacial isostasy and plate motion, *J. Geodyn.,* **46,** 95–103.

Komatitsch, D. & Tromp, J., 2002. Spectral-element simulations of global seismic wave propagation. Part I: validation, *Geophys. J. Int.* **149,** 390–412.

Lambeck, K. & Nakiboglu, S.M., 1980. Seamount loading and stress in the ocean lithosphere, *J. geophys. Res.,* **85,** 6403–6418.

Latychev, K., Mitrovica, J.X., Tamisiea, M.E., Tromp, J. & Moucha, R., 2005. Influence of lithospheric thickness variations on 3D crustal velocities due to glacial isostatic adjustment, *Geophys. Res. Lett.,* **32,** L01304.

Marotta, A.M. & Sabadini, R., 2004. The signatures of tectonics and glacial isostatic adjustment revealed by the strain rate in Europe, *Geophys. J. Int.,* **157,** 865–870.

Martinec, Z., 1999. Spectral, initial value approach for viscoelastic relaxation of a spherical Earth with a three-dimensional viscosity—I. Theory, *Geophys. J. Int.,* **137,** 469–488.

Martinec, Z., 2000. Spectral-finite element approach to three-dimensional viscoelastic relaxation in a spherical Earth, *Geophys. J. Int.,* **142,** 117–141.

Martinec, Z. & Wolf, D., 1999. Gravitational viscoelastic relaxation of eccentrically nested spheres, *Geophys. J. Int.,* **138,** 45–66.

Martinec, Z., Thoma, M. & Wolf, D., 2001. Material versus local incompressibility and its influence on glacial-isostatic adjustment, *Geophys. J. Int.,* **144,** 136–156.

McConnell, R.K., 1965. Isostatic adjustment in a layered Earth, *J. geophys. Res.,* **70,** 5171–5188.

Métivier, L., Greff-Lefftz, M. & Diament, M., 2006. Mantle lateral variations and elasto-gravitational deformations — I. Numerical modeling, *Geophys. J. Int.,* **167,** 1060–1076.

Okubo, S. & Endo, T., 1986. Static spheroidal deformation of degree 1— consistency relation, stress solution and partials, *Geophys. J. R. astr. Soc.,* **86,** 91–102.

Peltier, W.R., 1974. The impulse response of a Maxwell Earth, *Rev. Geophys. Space. Phys.,* **12,** 649–669.

Peltier, W.R., 1998. Postglacial variations in the level of the sea: implications for climate dynamics and solid-Earth geophysics, *Rev. Geophys.,* **36,** 603–689.

Peltier, W.R., 2004. Global glacial isostasy and the surface of the ice-age Earth: the ICE5G (VM2) model and GRACE, *Ann. Rev. Earth Planet. Sci.,* **32,** 111–149.

Plag, H.P. & Jüttner, H.U., 1995. Rayleigh-Taylor instabilities of a self-gravitating Earth, *J. Geodyn.,* **20,** 267–288.

Sabadini, R., Yuen, D.A. & Portney, M., 1986. The effects of upper-mantle lateral heterogeneities on postglacial rebound, *Geophys. Res. Lett.,* **13,** 337–340.

Saito, M., 1974. Some problems of static deformation of the Earth, *J. Phys. Earth,* **22,** 123–140.

Steffen, H., Kaufmann, G. & Wu, P., 2006. Three-dimensional finite-element modeling of the glacial isostatic adjustment in Fennoscandia, *Earth planet. Sci. Lett.,* **250,** 358–375.

Tanaka, Y., Okuno, J. & Okubo, S., 2006. A new method for the computation of global viscoelastic post-seismic deformation in a realistic earth model (I)—vertical displacement and gravity variation, *Geophys. J. Int.,* **164,** 273–289.

Tanaka, Y., Okuno, J. & Okubo, S., 2007. A new method for the computation of global viscoelastic post-seismic deformation in a realistic earth model (II)—horizontal displacement, *Geophys. J. Int.,* **170,** 1031–1052.

Tanaka, Y., Klemann, V. & Okuno, J., 2009. Application of a numerical inverse Laplace integration method to surface loading on a viscoelastic compressible Earth model, *Pure. appl. geophys.,* **166,** 1199–1216.

Tromp, J. & Mitrovica, J.X., 1999. Surface loading of a viscoelastic Earth-I. General theory, *Geophys. J. Int.,* **137,** 847–855.

Tromp, J. & Mitrovica, J.X., 2000. Surface loading of a viscoelastic Earth-III. Aspherical models, *Geophys. J. Int.,* **140,** 425–441.

Vermeersen, L.L.A. & Mitrovica, J.X., 2000. Gravitational stability of spherical self-gravitating relaxation models, *Geophys. J. Int.,* **142**(2), 351–360.

Vermeersen, L.L.A. & Sabadini, R., 1997. A new class of stratified viscoelastic models by analytical techniques, *Geophys. J. Int.,* **129,** 531–570.

Vermeersen, L.L.A., Sabadini, R. & Spada, G., 1996. Compressible rotational deformation, *Geophys. J. Int.,* **126,** 735–761.

Walcott, R.I., 1970. Isostatic response to loading of the crust of Canada, *Can. J. Earth Sci.,* **7,** 716–727.

Wang, R., 1991. *Tidal Deformations on a Rotating, Spherically Asymmetric, Visco-elastic and Laterally Heterogeneous Earth,* 139 pp., Peter Lang, Frankfurt.

Wang, H. & Wu, P., 2006a. Effects of lateral variations in lithospheric thickness and mantle viscosity on glacially induced relative sea levels and long wavelength gravity field in a spherical, self-gravitating Maxwell Earth, *Earth planet. Sci. Lett.,* **249,** 368–383.

Wang, H. & Wu, P., 2006b. Effects of lateral variations in lithospheric thickness and mantle viscosity on glacially induced surface motion on a spherical, selfgravitating Maxwell Earth, *Earth planet. Sci. Lett.,* **244,** 576–589.

Wang, H., Wu, P. & van der Wal, W., 2008. Using postglacial sea level, crustal velocities and gravity-rate-of-change to constrain the influence of thermal effects on mantle lateral heterogeneities, *J. Geod.,* **46,** 104–117.

Wessel, P. & Smith, W.H.F., 1991. Free software helps map and display data, *EOS, Trans. Am. geophys. Un.,* **72,** 441.

Whitehouse, P., Latychev, K., Milne, G.A., Mitrovica, J.X. & Kendall, R., 2006. Impact of 3D Earth structure on Fennoscandian glacial isostatic adjustment: implications for space-geodetic estimates of present-day crustal deformations, *Geophys. Res. Lett.,* **33,** L13502.

Wolf, D., 1985. The normal modes of a uniform, compressible Maxwell half-space, *J. Geophys.,* **56,** 100–105.

Wolf, D., 1991. Viscoelastodynamics of a stratified, compressible planet: incremental field equations and short- and long-time asymptotes, *Geophys. J. Int.,* **104,** 401–417.

Wolf, D., 1994. Lamé's problem of gravitational viscoelasticity: the isochemical, incompressible planet, *Geophys. J. Int.,* **116,** 321–348.

Wolf, D. & Kaufmann, G., 2000. Effects due to compressional and compositional density stratification on load-induced Maxwell viscoelastic perturbations, *Geophys. J. Int.,* **140,** 51–62.

Wolf, D. & Li, G., 2002. Compressible viscoelastic earth models based on Darwin's law, in *Ice Sheets, Sea Level and the Dynamic Earth,* pp. 275–292, eds Mitrovica, J.X. & Vermeersen, L.L.A., American Geophysical Union, Washington.

Wu, P. & Peltier, W.R., 1982. Viscous gravitational relaxation, *Geophys. J. R. astr. Soc.* **70,** 435–485.

Wu, P., 1999. Modelling postglacial sea levels with power-law rheology and a realistic ice model in the absence of ambient tectonic stress, *Geophys. J. Int.,* **139,** 691–702.

Wu, P., 2002. Mode coupling in a viscoelastic self-gravitating spherical Earth induced by axisymmetric loads and lateral viscosity variations, *Earth planet. Sci. Lett.,* **202,** 49–60.

Wu, P., 2004. Using commercial finite element packages for the study of Earth deformations, sea levels and the state of stress, *Geophys. J. Int.,* **158,** 401–408.

Wu, P., 2005. Effects of lateral variations in lithospheric thickness and mantle viscosity on glacially induced surface motion in Laurentia, *Earth planet.*

Sci. Lett., **235,** 549–563.

Wu, P. & Wang, H., 2008. Postglacial isostatic adjustment in a self-gravitating spherical Earth with power-law rheology, *J. Geodyn.,* **46,** 118–130.

Zhong, S., Paulson, A. & Wahr, J., 2003. Three-dimensional finite-element modelling of Earth's viscoelastic response: effects of lateral variations in lithospheric thickness, *Geophys. J. Int.,* **155,** 679–695.